A Revised Dislocation Model of Interseismic Deformation of the Cascadia Subduction Zone

— Preprint submitted as the final technical report for

USGS NEHRP Grant 01HQGR0058

Stress and Strain Regimes of the Pacific Northwest: A Comparative Study with S.W. Japan

Principle Investigators:
K. Wang, H. Dragert, and R. D. Hyndman

Pacific Geoscience Centre
9860 W Saanich Rd
Sidney, B.C.
Canada V8L 4B2

Tel: 250-363-6429
Fax: 250-363-6565
E-mail: wang@pgc.nrnca.gc.ca

A revised dislocation model of interseismic deformation of the Cascadia subduction zone

Kelin Wang[1,3], Ray Wells[2], Stephane Mazzotti[3,1], Roy D. Hyndman[1,3], and Takeshi Sagiya[4]

[1] Pacific Geoscience Centre, Geological Survey of Canada,
9860 West Saanich Road, Sidney, British Columbia V8L 4B2
Tel: (250)363-6429; fax: (250)-363-6565; e-mail: wang@pgc.nrcan.gc.ca

[2] U.S. Geological Survey, Menlo Park

[3] School of Earth and Ocean Sciences, University of Victoria

[4] Geographical Survey Institute, Tsukuba, Japan

Abstract. CAS3D-2, a new three-dimensional dislocation model, is developed to model interseismic deformation rates at the Cascadia subduction zone. The model is considered a snapshot description of the deformation field that changes with time. The effect of northward secular motion of the central and southern Cascadia forearc sliver is subtracted to obtain the effective convergence between the subducting plate and the forearc. Horizontal deformation data, including strain rates and surface velocities from Global Positioning System measurements, provide primary geodetic constraints, but uplift rate data from tide gauges and leveling also provide important validations for the model. A locked zone, based on the results of previous thermal models constrained by heat flow observations, is located entirely offshore beneath the continental slope. Similar to previous dislocation models, an effective zone of downdip transition from locking to full slip is used, but the slip deficit rate is assumed to decrease exponentially with downdip distance. The exponential function resolves the problem of over-predicting coastal GPS velocities and under-predicting inland velocities by previous models that used a linear downdip transition. A wide effective transition zone partially accounts for stress relaxation in the mantle wedge that cannot be simulated by the elastic model. The pattern of coseismic deformation is expected to be different from that of interseismic deformation at present, 300 years after the last great subduction earthquake. The downdip transition from full rupture to no slip should take place over a much narrower zone.

1. Introduction

Three hundred years have passed since the last great earthquake at the Cascadia subduction zone (Figure 1). The earthquake of 1700 generated tsunami waves that propagated across the Pacific Ocean to cause damage along the coast of Japan [Satake et al., 1996; Tsuji et al., 1998]. This earthquake probably ruptured the entire length of the Cascadia subduction fault, and the moment magnitude was estimated to be about 9 [Satake et al., 1996]. Paleoseismic studies by Atwater [1987] and many others (see summaries by Atwater and Hemphill-Haley [1997] and Clague [1997]), established that great earthquakes have repeatedly occurred along this continental margin with irregular intervals of a few hundred years.

Hyndman and Wang [1993] proposed that the updip and downdip limits of the seismogenic zone for a warm subduction zone such as Cascadia were controlled by temperature. At temperatures cooler than 100-150°C, the subduction fault may have a stable sliding behavior. Between 150°C and 350°C, the fault may exhibit seismogenic stick-slip behavior. Warmer than 350°C and through a transition zone, fault slip is expected to be stable. Thermal models for the Cascadia subduction zone [Hyndman and Wang, 1993, 1995] constrained by heat flow measurements showed that the 350°C isotherm is offshore beneath the continental slope. Despite various uncertainties in the model and geothermal data, the conclusion that the seismogenic zone as defined by the temperature limit is located far offshore is robust.

In the elastic dislocation model [Savage, 1983] (Figure 2), a shallow portion of the fault is assumed to be locked, and the fault is assumed to slip at the full plate convergence rate beyond a certain depth downdip. The slip deficit of the locked zone is recovered in future earthquakes. Given fault geometry and convergence rate, the model deformation depends only on the position and size of the locked zone and the transition between zones of no slip and full slip. After removing steady state plate convergence, assumed to cause no deformation, the locked portion of the fault can be equivalently described as slipping backwards, and the slip deficit becomes backslip. Because of the viscoelasticity of earth's mantle and because of the transient nature of fault motion, the rate of interseismic crustal deformation changes with time, generally faster just after a great earthquake and slower afterwards. The best example is the uplift rate variations before and after the 1944/46 great earthquakes along the Nankai subduction zone, as revealed by repeat leveling measurements [Thatcher, 1984; Miyashita, 1987]. The use of a static dislocation model does not necessarily imply a constant deformation rate between great earthquakes. The modeled deformation can be approximately considered a snapshot of a slowly changing deformation field. Based on a two-dimensional (2-D) dislocation model of Hyndman and Wang [1995], Flück et al. [1997] developed a three-dimensional (3-D) dislocation model for the Cascadia subduction zone, hereafter referred to as CAS3D-1. New GPS observations and new models for forearc motion and glacial rebound require that we revise the existing 3-D model. In this paper, we describe CAS3D-2, a revised 3-D dislocation model for Cascadia.

Similar expressions have been interchangeably used in the literature to describe the contact properties, the kinematics, or the state of stress of a subduction fault. For example, when a fault is said to be "strongly coupled", it is sometimes implied that not only is the fault locked, but also the shear stress must be high. The purely kinematic concept "seismic coupling", which describes the proportion of seismic vs. aseismic slip in long-term plate convergence, is sometimes misrelated to the level of stress. To avoid confusion, we explain some of our phrases in Table 1.

2. New Issues to be Addressed

2.1. Horizontal Deformation Data

CAS3D-1 used vertical deformation data as the primary model constraints, because horizontal deformation data were scarce. At the time, there were only two published GPS velocity vectors for the Cascadia margin. Six strain rate measurements were used, but four of them only provided shear strain estimates. The situation has been drastically improved in the past few years.

Figure 3b is a compilation of published velocities from GPS measurements. All velocities are relative to reference station DRAO at Penticton, British Columbia. Velocities obtained by different groups using different reference frames have been put into a common reference frame through simple transformations as explained by Mazzotti et al. [2002]. Velocity vectors obtained from campaign-style measurements were reported by Henton [2000] for British Columbia and by McCaffrey et al. [2000] and Savage et al. [2000] for Oregon. The Oregon results were reported relative to a stable North America defined in the original studies. Continuous GPS monitoring is provided by the Western Canada Deformation Array (WCDA) operated by the Geological Survey of Canada since 1991 and the PAcific Northwest Geodetic Array (PANGA) operated by a consortium of U.S. universities and government agencies since 1997. The vectors for the WCDA stations were reported by Henton [2000], and those for the PANGA stations by Miller et al. [2001]. Uncertainties in the GPS velocities vary from site to site, and formal statistical error ellipses may not adequately reflect uncertainties from all sources. Generally, velocities from continuous GPS stations that have been operating for more than four years are considered the most reliable. Campaign data are more vulnerable to errors depending on the total time span of the observations, the number of occupations of each station, the length of recording in each occupation, the change of receivers and antennas from one survey to the next, and the experience of the field workers.

The GPS vectors collectively represent the first-order pattern of crustal deformation of the Cascadia forearc. Several interesting features should be addressed by the new dislocation model. (1) Although there is a landward decrease in margin-normal velocities (or shortening in this direction), the decrease is not as fast as predicted by CAS3D-1. Henton [2000] found it difficult to explain the slow decrease observed across Vancouver Island simply by modifying the widths of the locked and transition zones of CAS3D-1. (2) The margin-normal component of the coastal sites are smaller than the CAS3D-1 predictions. McCaffrey et al. [2000] used a locked zone with a similar width to CAS3D-1 in Oregon but had to allow it to slip at 40-90% of the actual plate convergence rate. Similar phenomena are seen in other subduction zones, and the locked zone is often assumed to slip at some slow rate (sometimes called "partial coupling"; see Table 1). Aseismic slip of the seismogenic zone may happen from time to time [e.g., Heki et al., 1997], but it is yet to be resolved whether such slip can be a sustained continuous feature of interseismic behavior. (3) As one proceeds from north to south, the direction of the GPS velocities becomes more northerly. In southern Cascadia, the velocities of the coastal sites are much more oblique than predicted by any published plate models. This feature may reflect a continuous secular motion of the Cascadia forearc. As will be discussed in section 2.2, the effect of this motion should be subtracted if we wish to focus on interseismic deformation due to great earthquake cycles. Removing the secular motion introduces additional uncertainties to the affected GPS velocities, but strain rates locally derived from GPS velocities are little affected by this correction.

Figure 3 shows geodetic strain rate estimates in the Cascadia forearc up to year 2001. Strain rates for Canadian networks JST and GOL were reported by Dragert and Lisowski [1990], QCS and PAL by Dragert [1991], and CVI and SVI by Henton [2000]. Most of the strain rates in the United States part of the map were compiled or revised by Murray and Lisowski [2000]. Unnamed estimates shown in Figure 3 were derived by Mazzotti et al. [2002] from GPS velocities published by McCaffrey et al. [2000], Miller et al. [2001], and Henton [2000]. Early triangulation surveys provide precise measurement of angles but poor control of baseline lengths. Consequently, strain estimates based on repeated surveys where one or both surveys use triangulation are limited to shear strain only. Maximum contraction rates from such a combination of surveys are shown in Figure 3a under the assumption of uniaxial contraction.

2.2. Forearc Motion and Effects on Convergence Rate

Wells et al. [1998] synthesized paleomagnetic, neotectonic, gravity, and aeromagnetic observations in the Pacific Northwest and proposed a kinematic model of forearc motion (Figure 4). In this model, the southern Cascadia forearc, primarily the relatively rigid mafic Siletzia terrane in southern Washington and Oregon and the Klamath Mountains in northern California, moves northward and toward the Canadian coast mountains. The forearc also rotates clockwise as it moves north. Its motion relative to the stable North America (NA) plate can be well described as a rigid forearc sliver rotating around a Euler pole (Table 2). Figure 4 shows the position of the forearc-NA pole recently refined by Wells and Simpson [2001]. This model is supported by GPS observations [Savage et al., 2000; McCaffrey et al., 2000; Miller et al., 2001; Mazzotti et al., 2002]. The velocities in Figure 3b represent the combined effects of this secular forearc motion and interseismic strain accumulation. For example, as the area covered by the Oregon GPS network CAB (Figure 3a) moves northward and rotates clockwise, it is being shortened elastically in a nearly E-W direction. The maximum compressive stress is margin-parallel, but the margin-normal elastic contraction fluctuates throughout subduction earthquake cycles [Wang, 2000].

On a large scale, the rotating Cascadia forearc sliver can be considered the leading edge of the Basin and Range deformation [Magill et al., 1982]. As the Basin-and-Range spreads through gravitational collapse and is constrained by the right-lateral shear motion between the North America and Pacific (PA) plates, the weak Cascadia subduction zone provides a preferred direction of material flow, i.e., an "outlet" [Humphreys and Hemphill-Haley, 1996]. The low-heat-flow, cold forearc appears to act coherently, whereas to the east, deformation in the high heatflow arc and Basin and Range is diffuse [e.g., Pezzopane and Weldon, 1993].

The forearc motion affects the convergence direction and rate. There have been a number of plate convergence models for Juan de Fuca (JDF)-NA convergence. Figure 5a shows the JDF-NA convergence predicted by three of these models (Table 2). They all feature a southward decrease in convergence rate and increase in obliquity. The most recent model (solid arrows), used by McCaffrey et al. [2000] and Miller et al. [2001], is derived from the NUVEL-1A JDF-PA pole [DeMets et al., 1994; Wilson, 1993] and the PA-NA pole of DeMets and Dixon [1999]. The convergence rate of NUVEL-1 [DeMets et al., 1990] (white arrows in Figure 5a) evaluated at Seattle was uniformly applied to the entire margin in CAS3D-1 (white arrows in Figure 5b). With the recognition of the secular forearc motion (Figure 4), it now appears more reasonable to use the JDF-forearc convergence instead of JDF-NA convergence to model the interseismic forearc deformation.

We derive the JDF-forearc pole and rotation rate from the most recent JDF-NA pole (row three of Table 2) and the forearc-NA pole of Wells and Simpson [2001] and their rotation rates

(Table 2). The JDF-forearc pole applies to central and southern Cascadia. Assuming that the forearc sliver motion does not affect British Columbia (Figure 4), we directly use the convergence rate predicted by the JDF-NA pole for the northernmost part of the subduction zone. The region in between, bounded by the two dashed lines in Figure 5b, is assumed to have a linear transition from one convergence model to the other. The nearly uniform permanent long-term N-S shortening of the transitional area implied by this treatment contains large uncertainties, but it appears to hold up to the first order according to the deformation analysis of Mazzotti et al. [2002]. The resultant along-strike distribution of the effective convergence velocities, shown in Figure 5b (solid arrows), is used in CAS3D-2. Purely fortuitously, the direction of the JDF-forearc convergence and its uniformity in central and southern Cascadia are very similar to what was used in CAS3D-1 (Figure 5b), which explains why CAS3D-1 appears to give reasonable results in explaining the interseismic deformation in that region [Murray and Lisowski, 2000].

To allow meaningful comparisons between model and data, the secular forearc motion (Figure 4) needs to be accounted for; we have chosen to remove it from the observed displacements. GPS velocities after removing the forearc motion are shown in Figure 3c. Removing a rigid-body component of the deformation field does not affect local strain rate estimates. A small correction to the strain rates in the transitional area can also be made, but considering the ad hoc fashion of defining the transition and the small size of the affected area, such a correction is deemed unimportant.

2.3. Re-evaluation of Post-glacial Rebound and Vertical Deformation

Vertical deformation observations contain relatively large uncertainties. Most of the previously published leveling and tide gauge data, when used by Dragert et al. [1994], Hyndman and Wang [1995], and the CAS3D-1 modeling of Flück et al. [1997], were corrected for the effect of post-glacial rebound. After the retreat of the Laurentide ice sheet at the end of the Pleistocene, initially depressed northern North America experienced a gradual uplift. The rate and spatial pattern of the uplift depend on the original ice thickness, deglaciation history, the effective elastic thickness of the lithosphere, and the viscosity of the underlying mantle. The best post-glacial rebound models then available were ICE-3G [Tushingham and Peltier, 1991] and ICE-4G [Peltier, 1994]. These models were designed to model the global-scale post-glacial rebound process and were constrained by data primarily from the stable continental interior. ICE-3G and ICE-4G feature a 120 km thick elastic lithosphere and a viscosity of 10^{21} Pa s for the upper mantle, perhaps appropriate for the continental interior. According to these global models, the Cascadia forearc, especially its northernmost portion, should still be strongly affected by post-glacial rebound today. For example, a seaward tilt of the Vancouver Island, with its west coast subsiding relative to its east coast at about 1.2 mm/yr, was predicted by these models. Removing this model-predicted post-glacial rebound signal added a landward tilt (Figure 6). Similar but smaller corrections were made by Hyndman and Wang [1995] to tide gauge data from Washington, Oregon, and California.

New studies have shown that the post-glacial rebound land tilt is negligible. James et al. [2000] conducted a post-glacial rebound analysis of the northern Cascadia margin, using a detailed regional deglaciation history. The local rebound model was constrained by shore line tilts of pro-glacial lakes in Washington and relative sea level changes in southern British Columbia. Fitting these data to a model of an elastic plate overlying a viscoelastic sub-lithospheric mantle, they inferred a much thinner elastic plate (< 40 km) and a much lower mantle viscosity (~ 10^{19} Pa s) and therefore a much faster post-glacial rebound than predicted by

the global rebound models for this region. Consequently, James et al. [2000] concluded that there was no longer appreciable land tilt due to rebound at present. Using a slightly more refined model, Clague and James [2002] confirmed the conclusion of James et al. [2000], but added that there was at present a nearly uniform uplift of the northern Cascadia margin at about 0.5 mm/yr.

Dropping post-glacial rebound land-tilt corrections simplifies the analysis of vertical deformation, but complications have arisen from a different source. From relative sealevel change observations using marine terraces, Friele and Hutchinson [1993] and Hutchinson et al. [2000] noticed that there had been a general uplift of the west coast of Vancouver Island relative to the Fraser lowland at an average rate of about 1-1.5 mm/yr for the past few thousand years. This means that much of our observed landward tilt (Figure 6, without post-glacial corrections) may be due to a long-term process. This regional tilt has a much larger time scale than great earthquake cycles but cannot be explained by any post-glacial rebound models. It probably reflects a plate boundary tectonic process that is not presently understood. It is possible that this type of long-term vertical deformation varies along strike, independent of fault locking and unlocking. Long-term net uplift or subsidence has been observed at other subduction zones, and explanations have been site-specific or *ad hoc*. For example, long-term uplift has been observed at Cape Muruto in the Nankai forearc, which has been explained either by an intrinsic asymmetry of earthquake deformation cycles [Sato and Matsu'ura, 1992] or by margin-parallel neotectonic processes [Sugiyama, 1994].

2.4. Nature of the Downdip Transition Zone

Transition zones in elastic dislocation models (Figure 2) are used because it is not physically plausible to allow fault slip to change abruptly from zero to the full plate convergence rate. Because we are using a static elastic model to approximate a time dependent process, the transition zone is largely a mathematical convenience. We call the transition zone that we infer from the elastic model an "effective transition zone" (ETZ). In a real subduction zone, the surface deformation, especially at a time as long as 300 years after a great earthquake, is controlled by the slow (viscous) deformation of the mantle wedge as well as the locking and slipping of the subduction fault. In the elastic model, all is attributed to the fault. The "effective transition zone" is meaningful and useful in much the same way as the concept of the "effective elastic thickness" of the lithosphere and numerous other geophysical concepts that characterize integrated effects of many controlling factors using a single parameter.

Scholz [1990] proposed that a transition from the seismogenic stick-slip behavior to stable-sliding took place over a temperature range along a fault. Hyndman and Wang [1993] suggested that for warm subduction zones like Cascadia, the transition might be between 350°C and 450°C. It is reasonable to assume that the stick-slip segment is locked between earthquakes, but stable-sliding behavior does not mean that the fault must be sliding at the plate convergence rate (Table 1).

Two characteristics can be expected of the ETZ of a subduction fault. (1) Because the ETZ also accounts for the effect of the mantle wedge, it is not expected to have a sharp downdip end. The backslip rate near the downdip end of the transition zone should taper more gradually than what is described by a linear transition. Unlike the updip limit of the ETZ that is controlled by a change from stick-slip to stable-sliding behavior, there may not be a property contrast to define the downdip end. (2) The width and slip distribution of the ETZ likely evolve with time during the interseismic period. The deeper stable-sliding part of the fault resists rapid coseismic slip, but it will catch up with the rupture zone by slipping aseismically after the earthquake. Thus after a great earthquake and the re-locking of the fault, the transition zone between no-slip to full-slip

should gradually widen with time. The viscoelastic behavior of the mantle wedge between the two converging plates leads to the same effect. Its coseismic elastic response resists shear and tends to confine crustal deformation within the proximity of the rupture area. For some time after the earthquake, stress relaxation in the mantle allows crustal deformation to be distributed over a wider area [Wang, 1995]. In an elastic dislocation model, the relaxation of the mantle wedge translates to a widening ETZ. Therefore, it is expected that the ETZ 300 years after the great earthquake is much wider than a transition zone shortly, e.g., 50 years, after the earthquake. A silent slip event on the Cascadia plate interface at about 30 to 40 km depth in 1999 [Dragert et al., 2001] reveals the complexity of the ETZ and its larger width than previously thought.

In a 3-D viscoelastic model of Cascadia interseismic deformation, Wang et al. [2001] used a thin viscoelastic layer overlapping a kinematically defined zone of linearly decreasing backslip to approximate the stable-sliding part of the subduction fault. The modeled deformation 300 years after a great earthquake well agrees with GPS velocities in northern Cascadia and most strain rate observations in the rest of the forearc, although the viscoelastic model did not account for the effect of forearc motion in central and southern Cascadia. The fault slip rate across southern Vancouver Island as seen in this model is shown in Figure 7 as an example to demonstrate the two points in the preceding paragraph. The kinematically defined zone of decreasing slip deficit is between 60 km and 120 km distance. Shortly after the earthquake, the stable-sliding part of the fault immediately downdip of the coseismic rupture slips faster than plate convergence (slip deficit < 0), and the width of the transition zone is about 60 km. 300 years after the earthquake, the transition zone is about 100 km and the downdip termination is very gradual and hence not well defined. If the additional mantle relaxation effect in the viscoelastic model is to be represented by a transition zone in an elastic model, the width of the transition zone at 300 years has to be even larger.

In light of the above discussions, we decide to use an ETZ for CAS3D-2 that is wider than in CAS3D-1 and has an exponentially decreasing downdip slip distribution. The width of the zone and the exact shape of the slip distribution are to be constrained by deformation observations. Mathematical details will be given in the following section.

3. CAS3D-2

3.1. The Effective Transition Zone

CAS3D-2 employs the following backslip (i.e., slip deficit) distribution as a function of downdip distance x from the updip end of the ETZ:

$$s = s_o \frac{\exp(-x/\gamma) - \exp(-w/\gamma)}{1 - \exp(-w/\gamma)}, \qquad (1)$$

where s_o is the plate convergence rate (i.e., full backslip rate of the locked zone), w is the width of the ETZ, and γ is a parameter controlling the shape of the slip distribution. Within the ETZ ($0 \le x \le w$), the slip rate decreases at a greater rate near the updip end and at a lower rate further downdip; $s = 0$ for $x > w$. For a very small γ, all the decrease takes place near $x = 0$, like a step function. For a large γ, s changes linearly from s_o to zero over the ETZ. The function is illustrated in Figure 8 for three different values of γ. Both w and γ vary with the time lapsed from the previous earthquake and may vary along strike. For simplicity, we use a uniform γ for

CAS3D-2, although we allow w to vary along strike.

In terms of the seismogenic properties of the fault, there may be a seaward zone of transition from stick-slip to stable-sliding behavior. Although the thermal conditions allow the entire shallow portion of the fault to be seismogenic [Hyndman and Wang, 1993], there may be other factors that make some shallow portion aseismic. However, even if there is a seaward portion of the fault that is not locked at present, we are not able to tell from land geodetic measurements. If most of the seismogenic zone is locked, the upper slippery segment, if present, is not able to move by itself (except perhaps for a very short time after a great earthquake). Therefore kinematically, that portion is a part of the locked zone.

3.2. Model Assumptions and Constraints

3.2.1. Thermal constraints to the locked zone. Land geodetic data do not resolve the precise position of the locked zone if it is far offshore. Therefore, as in CAS3D-1, we assume that the locked zone is defined by temperature limits. The 350°C downdip limit for the seismogenic zone has been tested at the warm Nankai subduction zone where there have been recent great earthquakes [Hyndman et al., 1995]. The thermal limits indicate that earthquakes are unlikely to be generated outside the seismogenic zone, but they do not imply that every great earthquake must rupture the entire seismogenic zone.

3.2.2. Strain rate observations. Strain rate estimates are not affected by reference frame uncertainties and the removal of the rigid-body motion of the forearc sliver. Strain rate tensor estimates (Figure 3a) which became available for Cascadia only for the past decade are considered the best constraints for interseismic elastic strain accumulation. Shear strain rate estimates (Figure 3a) that involved early triangulation surveys provide averages over time periods of several decades, whereas estimates of strain tensors tend to be averages over several (and more recent) years. The shear strain estimates generally show a shortening rate greater than the later strain rate tensor estimates. Although strain rate is expected to decrease with time in the interseismic period, as predicted by viscoelastic models [Wang et al., 2001], it is not clear whether the observed difference reflects entirely a temporal change or also a difference in technology-related measurement accuracy. For a model of contemporary deformation, we give more weight to the more recent and better quality strain tensor data. Quantitative measures of model fit are applied only to the strain tensor data. Visual comparison of model results with GPS velocities and uplift data is made to provide additional constraints.

3.2.3. GPS velocities not affected by forearc motion. The large uncertainties in the pole position for the forearc sliver as represented by the error ellipse in Figure 4, rotation rate, and the assumption of rigid block motion all introduce uncertainties when the secular forearc motion is removed from the GPS observations. Forearc GPS vectors north of the northern Washington transitional area in Figure 5b are little or not affected by the secular motion [Wells et al., 1998] and are considered good model constraints. GPS velocities do not contain exactly the same information as strain rate data. The strain estimates were made from relative position changes between nearby sites within small networks and represent local deformation. The GPS velocities in Figure 3 represent the position changes between the observation sites and reference station DRAO.

3.2.4. GPS velocities affected by forearc motion. The forearc-NA pole and rate that we use were obtained from geological observations [Wells and Simpson, 2001]. Using GPS data alone, McCaffrey et al. [2000] obtained a similar pole position, but Savage and Svarc (personal communication, 2001) obtained a different pole. Although the long-term geologic pole is less precise, it is not affected by short-term perturbations and is compatible with the large-scale,

regional geological deformation history. The forearc-motion component that we remove from Oregon GPS velocities is generally larger than the component of interseismic deformation (Figure 3b,c) that we use as signal. A slight error in the description of the forearc motion may result in large uncertainties in the small residual that represent interseismic deformation.

3.2.5. Vertical deformation data. For reasons explained in Section 2.3, the post-glacial rebound correction for a land tilt is no longer considered necessary. Instead, the tide gauge data are corrected only for a small vertical uplift rate predicted by the post-glacial rebound model of Clague and James [2002]. This small correction makes the tide gauge uplift rate in northern Cascadia almost uniformly smaller by about 0.5 mm/yr. U.S. leveling data used by CAS3D-1 were not acquired for tectonic studies, but the measurements made in 1987 were of sufficiently good quality (see summary by Hyndman and Wang [1995]) and, in conjunction with surveys made in the 1930's, yield good land tilt rates along three profiles (Figure 1). Leveling data obtained in the period of 1930-1941 are subject to very large uncertainties. Given that much more horizontal deformation data are available, it is no longer a substantial loss to exclude the leveling line segments where measurements were made only in this period. Date from two leveling lines across Vancouver Island, detailed by Dragert et al. [1994], are of better quality. Land tilt along the Tofino leveling line (Figure 1) is shown in Figure 6. Vancouver Island appears to experience a yet unexplained long-term land tilt (Figure 6), but there has been no evidence for this effect for the rest of the margin.

3.3. Fault Geometry

A 3-D geometry of the Cascadia subducton fault was compiled by Flück et al. [1997] and used for CAS3D-1 and a number of subsequent studies by various groups. Some improvements have been made in constraining the fault geometry, but the improvements are in the depth of the slab landward the coast [e.g., Trehu et al., 2002]. The offshore seismogenic part of the fault remains unchanged. The fault landward of the coast is more than 15 km deep and includes only the waning part of the ETZ (Section 3.6), so its exact geometry is not critical to surface deformation. Therefore, CAS3D-2 uses the same fault geometry as CAS3D-1. The fault is represented by 16 cross-sectional profiles. To allow the flat free surface in the model to represent the seafloor and land surface, a correction is made for the land-seafloor topographic relief. The fault depth is adjusted accordingly so that the topography correction does not change the depth of the fault, as explained by Flück et al. [1997]. Along each profile, the topographically corrected downdip geometry is approximated to be circular. The profiles are connected by along-strike straight lines.

3.4. Backslip Distribution

In CAS3D-2, the plate convergence rate and direction vary along strike (Section 2.2 and Figure 5b). The backslip rate at a given point in the locked zone is calculated as follows (Figure 9a). For any given point F on the fault, we first determine the relative plate convergence vector v_s at surface point S directly above F, using the appropriate Euler pole(s), that is, the JDF-forearc pole for central and southern Cascadia, the JDF-NA pole for northernmost Cascadia, and a linear transition between the two in northern Washington (Figure 5b). Vector v_s is then rotated around the local strike of the fault to the fault plane to give the slip vector v_f. A precise determination of v_s should be made at point S', where F would be if the fault were restored to a flat shape (Figure 9b), but the direct local projection is a good approximation for small average fault dip α. If F is at a normal distance x from the trench (point T), and the rate of change in v_s along line T-F is r =

dv_f/dx, the error in v_f introduced by this procedure is $xr(1 - \cos\alpha)/\cos\alpha$. Unless the Euler pole is very close, r is very small. Thus very little error is introduced for the shallow-dip seismogenic portion of a subduction fault. The backslip vector in the ETZ is calculated in the same way but is scaled using the exponential function of (1).

3.5. Calculation Method

The method of calculation of surface deformation from the pattern of backslip on the fault has been explained in Flück et al. [1997]. The model is a uniform elastic half-space with a flat surface, and the Poisson's ratio is 0.25 (such that the ratio of the two Lame constants is unity). Variable slip rates and directions are assigned to the curved fault as point-source edge dislocations. The solution for displacement and strain at a surface point caused by each point source was given by Okada [1985]. The total displacement and strain at a surface point are obtained by numerically integrating contributions from all the point sources over the entire fault. Except for strain rate tensors, comparison of model results with geodetic observations is made largely on a trial-and-error basis. Because the locked zone is assumed to be thermally constrained, little attempt was made to adjust its width. The width w of the ETZ and the shape factor γ are adjusted to fit geodetic observations.

3.6. Model Results

The best-fit slip deficit model is shown in Figure 10. The strain rates, velocities relative to DRAO, and uplift rates calculated using CAS3D-2 are shown in Figure 11 and compared with observations. The results for the 100 km of the northern and southern parts of the subduction zone may be a poor approximation, because the dislocation model is not intended to describe the complex crustal deformation near triple junctions. A measure of the model fit is the root-mean-square (RMS) misfit to the rates and directions of maximum contraction for the strain rate tensors near the coast (strain rates near the volcanic arc or in the back-arc region are potentially affected by other processes). For the w distribution shown in Figure 10, the RMS misfit as a function of γ is shown in Figure 12. A γ value of 0.5 provides a compromise between the best fits for the rates and directions. Larger γ values are also acceptable by the strain rates, but the results would compare poorly the limited uplift rate observations.

The region of the locked zone (Figure 11, dark shading) is similar to that of CAS3D-1. A shape factor $\gamma = 0.5$ for the transition zone (Figure 8) is found to give a reasonable model fit to the data. The effective transition zone is about twice as wide as in CAS3D-1, but because of the exponential distribution defined in (1), 3/4 of the backslip rate decrease takes place in its seaward half (intermediate shading), and the backslip rate is very small in the landward half (light shading). CAS3D-2 assumes a faster backslip-rate decrease in the transition zone of CAS3D-1 but has the slip at slow rates farther landward. The initial faster decrease results in a lower velocity at the coastal GPS sites, and therefore we do not need to assume the locked zone to be slowly slipping. The landward extension of the transition zone allows surface velocities to decrease more slowly landward than predicted by CAS3D-1, resulting in a smaller margin-normal contraction. The kinematic dislocation model does not give a physical explanation for the form of the effective transition zone, but we believe that w or γ, or both, would have been smaller earlier in the interseismic period (see Section 2.4 above).

The model provides a good fit to the strain rate tensor data away from the triple junctions (Figure 11a). The (earlier) shear strain measurements are consistent with the tensor data in the overall direction of margin-normal contraction but have a greater scatter.

The model provides a better fit to the GPS velocities in Vancouver Island than CAS3D-1 or its variations [Henton, 2000] (Figure 11b). Despite the large uncertainties in the secular forearc motion, the GPS velocities in central and southern Cascadia are reasonably well fit by the model. Inland GPS sites in southern Oregon near the Cascadia volcanic arc are likely affected by processes other than interseismic elastic deformation. Northern California has few GPS measurements, and the complex secular deformation associated with the San Andreas transform plate boundary is not well described by the forearc motion model of Figure 4. The large northern component of the GPS velocity at Cape Mendocino probably represents PA-NA shear more than JDF-Cascadia convergence.

The CAS3D-2 model predicts a more gentle landward tilt than CAS3D-1. The west coast of Vancouver Island uplifts relative to the Fraser lowland region by about 1 mm/yr. The tide gauge data shown in Figure 11c have been corrected for a nearly uniform uplift of about 0.5 mm/yr concluded by Clague and James [2002] but not for the less understood long-term landward tilt observed by Hutchinson et al. [2000] (see Section 2.3 and Figure 6). The differential uplift between the west coast of Vancouver Island and Fraser lowland reported by Hutchinson et al. [2000] is about 1-1.5 mm/yr. If this long-term tilt is removed from the tide gauge data, the residual uplift pattern agrees with the dislocation model results quite well. The same is true for the leveling data across Vancouver Island (Figure 6). Not all U.S. tide gauges reported by Mitchell et al. [1994] were used by CAS3D-1 and CAS3D-2 (see Hyndman and Wang [1995] for explanations). Observed and model predicted uplift rates along the Coquille-Dillard and Arcata-Redding leveling lines are shown in Figure 13. The model is in disagreement with vertical deformation data from central Oregon, where the Newport-Albany leveling line shows no land tilt (data not reproduced here), and a nearby tide gauge shows no uplift. There is likely some other process that affects vertical deformation in central Oregon [McNeill et al., 2000]. Except in central Oregon, the model is generally consistent with the observed uplift pattern.

The much wider locked and transition zones in the Olympic Peninsula, Vancouver, Victoria, and Seattle region are associated with the shallower dip of the subduction fault. The shallow dip is probably caused by the "warping" of the slab at the corner of the subduction zone [Rogers, 1983]. If other parameters are similar, a shallower dip results in a wider seismogenic zone [Hyndman and Wang, 1993]. As discussed above, the location and width of the locked zone are based primarily on thermal arguments and supported by deformation observations, but the width and slip distribution of the transition zone are constrained by deformation data alone.

4. On Coseismic Deformation

For estimating ground shaking and hazards, it is the coseismic rupture that is important. Because of viscoelasticity, interseismic and coseismic deformation cannot be symmetric. The "softer" parts of the subduction system, such as the mantle wedge and the velocity-strengthening (similar to being viscous) part of the fault, do not allow widely distributed coseismic deformation but do allow widely distributed interseismic deformation [Wang, 1995]. We also know this from observations. The coseismic and interseismic deformation patterns as shown by a number of leveling surveys 50 years before through 30 years after the 1944/1946 great Nankai subduction earthquakes are far from being symmetric [Thatcher, 1984; Miyashita, 1987]. The current uplift pattern (Sagiya, unpublished data), over half a century after the earthquakes, is not a mirror image of the coseismic deformation pattern. If the evolution of interseismic deformation were to be approximated by a series of snapshot elastic dislocation models, we would need to use a narrower effective transition zone shortly after the earthquake but a wider one sometime

later. Therefore, if coseismic deformation is represented by reversing the interseimic deformation pattern, the width of the rupture zone will usually be over-estimated, especially if the interseismic deformation is observed a long time (such as 300 years) after the previous earthquake.

There are no coseismic seismological or geodetic observations to constrain the coseismic rupture zone. Tsunami heights in Japanese historical records can constrain the slip distance of the 1700 Cascadia earthquake [Satake et al., 1996] but do not well constrain the downdip limit of the rupture. The thermally defined seismogenic zone is where the earthquake may nucleate, but the actual rupture may extend into the transition zone. To estimate the potential rupture zone, we need to consider knowledge acquired from other subduction zones and paleoseismic evidence for coseismic deformation of the 1700 Cascadia earthquake. Inversion of geodetic data [Sagiya and Thacther, 1999] and tsumani waves forms [Tanioka and Satake, 2001] indicates that maximum coseismic rupture of the 1944/1946 Nankai great earthquakes occurred near the base of the thermally inferred locked zone and that the fault slip decreases downdip to a distance about half of the width of the locked zone. A wider (downdip) interseismically locked zone corresponds to a wider coseismic rupture zone.

A conservative approach for Cascadia is to assume that full coseismic rupture takes place over the entire locked zone and the slip decreases linearly downdip half-way into the present effective transition zone. Assuming 500 years of slip deficit (about 18 m) is recovered in one earthquake, we calculate the vertical coseismic deformation (Figure 14). Cascadia paleoseismic data cannot yet constrain 1700 coseismic deformation accurately but can provide minimum coastal subsidence at several locations along the coast. The estimates shown in Figure 14 are based on the results of Guilbault et al. [1996], Shannon et al. [1996, 1998], Atwater and Hemphill-Haley [1997], and Peterson et al. [1997]. Although there is general agreement between model and data in Figure 14, there are large uncertainties in the assumed coseismic rupture scenario. The paleoseismic data may contain post-seismic deformation and thus may not be truly coseismic. The recurrence interval of Cascadia great earthquakes is variable, and 500 years is only a convenient average [Atwater and Hemphill-Haley, 1997]. In addition, heterogeneous friction properties and pore fluid pressure distribution may cause different parts of the seismogenic zone to rupture in different earthquakes. Much future work is needed to improve paleoseismic coseismic deformation estimates and to learn from great earthquakes that are observed at other subduction zones.

5. Conclusions

Four reasons prompted a revision of a previously developed 3-D dislocation model (CAS3D-1) for the contemporary, interseismic deformation of the Cascadia subduction zone: (1) The rapid development of GPS observations has provided much better constraints on the horizontal interseismic deformation. (2) Geological studies and GPS observations have provided a much better understanding of the kinematics of the secular northward motion and clockwise rotation of the forearc sliver of central and southern Cascadia. It is the convergence between the subducting JDF plate and the migrating overriding forearc that control the interseismic forearc deformation. (3) New post-glacial rebound analyses and neotectonic observations have modified our view of the vertical deformation of the Cascadia margin. (4) New modeling and observational studies have improved our understanding of the time dependence of interseismic deformation and the nature of the effective transition zone employed by the elastic dislocation model.

The new 3-D dislocation model CAS3D-2 is constrained by (1) the thermally defined updip and downdip limits of the locked zone of subduction faults, (2) horizontal strain rate observations, (3) GPS velocities in northern Cascadia unaffected by the secular motion of the forearc sliver, (4) GPS velocities in central and southern Cascadia after a correction for the secular forearc motion, and (5) the general uplift rate pattern constrained by tide gauges along the coast and leveling data from Vancouver Island, Oregon, and California.

CAS3D-2 gives a locked zone that is very similar to CAS3D-1, retaining the same feature of being wider off the Olympic Peninsula and narrower to the north and south. An effective transition zone is employed to allow a downdip decrease in slip deficit along the fault and to account for the effect of viscoelastic relaxation of the mantle wedge in an elastic model. In the effective transition zone, slip deficit (backslip) rate has been approximated by an exponential function, which allows a faster decrease in the backslip rate in the seaward half of the transition zone and slower in the landward half. The downdip limit of the effective transition zone is not defined by fault properties and the width should increase with time. At present, 300 years after a great earthquake, the total width is about twice the width of the locked zone. The new model resolves the problem of over-predicting velocities of the costal GPS sites and under-predicting inland velocities in previous models. The new model predicts a much smaller landward tilt of the forearc, consistent with the newly interpreted uplift observations. Coseismic deformation is expected to have a narrower transition zone than the interseismic deformation 300 years after an earthquake.

Acknowledgments. We thank R. McCaffrey and M. Miller for making the U.S. GPS data available, and H. Dragert, J. Henton, M. Schmidt, and Y. Lu for cooperative efforts in collecting the Canadian GPS data. P. Flück wrote the initial version of the FORTRAN program DISL3D and participated in some of the later modifications. Y. Okada kindly provided his subroutine for calculating the surface deformation due to a point-source dislocation. B. Atwater pointed us toward the references that provide paleoseismic estimates of coastal coseismic subsidence and explained the uncertainties in the estimates. T. Dixon, H. Dragert, J. Freymueller, P. Lundren, W. Prescott, and J. Savage provided valuable comments on earlier versions of the manuscript. SM is supported by the Canadian GEOIDE project. The work is partially supported by the USGS NEHRP grants 00HQGR0061 and 01HQGR0058. Geological Survey of Canada contribution xxxxxx.

References

Atwater, B. F., Evidence for great Holocene earthquakes along the outer coast of Washington State, *Science, 236*, 942-944, 1987.

Atwater, B. F., and E. Hemphill-Haley, Recurrence intervals for great earthquakes of the past 3500 years at northeastern Willapa Bay, Washington, *U.S. Geological Survey Professional Paper, 1576*, 108 pp., 1997.

Clague, J., Evidence for large earthquakes at the Cascadia subduction zone, *Rev. Geophys., 35*, 439-460, 1997.

Clague, J., and T. S. James, History and isostatic effects of the last ice sheet in southern British Columbia, *Quat. Sci. Rev., 21*, 71-87, 2002.

DeMets, C. and T. H. Dixon, New kinematic models for Pacific - North America motion from 3 Ma to present, I: Evidence for steady motion and biases in the NUVEL-1A model, *Geophys. Res. Lett., 26*, 1921-1924, 1999.

DeMets, C., R.G. Gordon, D.F. Argus, and S. Stein, Current plate motions, *Geophys. J. Int., 101*,

425-478, 1990.

DeMets, C., R.G. Gordon, D.F. Argus, and S. Stein, Effects of recent revisions to the geomagnetic reversal time scale on estimates of current plate motions, *Geophys. Res. Lett., 21*, 2191-2194, 1994.

Dragert, H., Recent horizontal strain accumulation on Vancouver Island, British Columbia (abstract), *Eos, Trans. AGU, 72, Fall meeting suppl., 314*, 1991.

Dragert, H. and M. Lisowski, Crustal deformation measurements on Vancouver Island, British Columbia: 1976 to 1988, in *Global and regional geodynamics*, Edited by P. Vyskocil, C. Reigber, and P. A. Cross, Springer-Verlag, New York, 1990.

Dragert, H., R. D. Hyndman, G. C. Rogers, G. C. and K. Wang, Current deformation and the width of the seismogenic zone of the northern Cascadia subduction thrust, *J. Geophys. Res., 99*, 653-668, 1994.

Dragert, H., K. Wang, and T. S. James, A silent slip event on the deeper Cascadia subduction interface, *Science, 292*, 1525-1528, 2001.

Friele, P. A., and I. Hutchinson, Holocene sea-level change on the central west coast of Vancouver Island, British Columbia, *Can. J. Earth Sci., 30*, 832-840, 1993.

Flück, P., R. D. Hyndman, and K. Wang, Three-dimensional dislocation model for great earthquakes of the Cascadia subduction zone. *J. Geophys. Res., 102*, 20,539-20,550, 1997.

Guilbault, J.-P., J. J. Clague, and M. Lapointe, Foraminiferal evidence for the amount of coseismic subsidence during a late Holocene earthquake on Vancouver Island, west coast of Canada, *Quat. Sci. Rev., 15*, 913-937, 1996.

Heki, K., S. Miyazaki, and H. Tsuji, Silent fault slip following an interplate thrust earthquake at the Japan Trench, *Nature, 386*, 595-598, 1997.

Henton, J. A., GPS Studies of Crustal Deformation in the Northern Cascadia Subduction Zone, Ph.D. thesis, University of Victoria, British Columbia, 2000.

Humphreys, E., and M. A. Hemphill-Haley, Causes and characteristics of western U. S. deformation, *Geol. Soc. Am. Abstracts, 28*, 1996.

Hutchinson, I., J.-P. Guilbault, J. J. Clague, and P. T. Bobrowsky, Tsunamis and tectonic deformation at the northern Cascadia margin: a 3000-year record from Deserted Lake, Vancouver Island, British Columbia, Canada, *The Holocene, 10*, 429-439, 2000.

Hyndman, R. D. and K. Wang, Thermal constraints on the zone of major thrust earthquake failure, The Cascadia subduction zone, *J. Geophys. Res., 98*, 2039–2060, 1993.

Hyndman, R. D. and K. Wang, Current deformation and thermal constraints on the zone of potential great earthquakes on the Cascadia subduction thrust, *J. Geophys. Res., 100*, 22,133-22,154, 1995.

Hyndman, R. D., K. Wang, and M. Yamano, Thermal constraints on the seismogenic portion of the southwestern Japan subduction thrust, *J. Geophys. Res., 100*, 15,373-15,392, 1995.

James, T. S., J. J. Clague, K. Wang, and I. Hutchinson, Postglacial rebound at the northern Cascadia subduction zone, *Quat. Sci. Rev., 19*, 1527-1541, 2000.

Magill, J. R., R. E. Wells, R. W. Simpson, and A. V. Cox, Post-12 m.y. rotation of Southwest Washington, *J. Geophys. Res., 87*, 3761-3776, 1982.

Mazzotti, S., H. Dragert, R. D. Hyndman, M. M. Miller, and J. A. Henton, GPS deformation in a region of high crustal seismicity: N. Cascadia forearc, *Earth Planet. Sci. Lett., 198*, 41-48, 2002.

McCaffrey, R., M. D. Long, C. Goldfinger, P. C. Zwick, J. L.Nabelek, C. K. Johnson and C. Smith, Rotation and plate coupling along the southern Cascadia subduction zone, *Geophys. Res. Lett, 27*, 3117-3120, 2000.

McNeill, L. C., C. Goldfinger, L. V. D. Kulm, and R. Yeats, Tectonics of the Neogene Cascadia

forarc basin: Investigations of a deformed late Miocene unconformity, *Geol. Assoc. Am. Bull., 112*, 1209-1224, 2000.

Miller, M. M., D. J. Johnson, C. M. Rubin, H. Dragert, K.Wang, A. Qamar and C. Goldfinger, GPS-determination of along-strike variation in Cascadia margin kinematics: Implications for relative plate motion, subduction zone coupling, and permanent deformation, *Tectonics, 20*, 161-176, 2001.

Mitchell, C. E., P. Vincent, R. J. Weldon II, and M. A. Richards, Present-day vertical deformation of the Cascadia margin, Pacific Northwest, United States, *J. Geophys. Res., 99*, 12,257-12,277, 1994.

Miyashita, K, A model of plate convergence in Southwest Japan, inferred from levelling data associated with the 1946 Nankaido earthquake, *J. Phys. Earth, 35*, 449-467, 1987.

Murray, M. H., and M. Lisowski, Strain accumulation along the Cascadia subduction zone, *Geophys. Res. Lett., 26*, 3631-3634, 2000.

Okada, Y., Internal deformation due to shear and tensile faults in a half space, *Bull. Seismol. Soc. Am., 82*, 1018-1040, 1992.

Peltier, W. R., Ice age paleotopography, *Science, 265*, 195-201.

Peterson, C. D., E. T. Barnett, G. G. Briggs, G. A. Carver, J. J. Clague, and M. E. Darienzo, Estimates of coastal subsidence from great earthquakes in the Cascadia subduction zone, Vancouver Island, B.C., Washington, Oregon and northermost California: Oregon Department of Geology and Mineral Industries Open-file Report 0-97-05, 24 p., 1997.

Pezzopane, S. K. and R. J. Weldon II, Tectonic role of active faulting in central Oregon, *Tectonics, 12*, 1140-1169, 1993.

Riddihough, R., Recent movements of the Juan de Fuca plate system. *J. Geophys. Res., 89*, 6980-6994, 1984.

Rogers, G. C., Seismotectonics of British Columbia, Ph.D. thesis, University of British Columbia, Vancouver, British Columbia, 247 pp., 1983.

Sagiya, T., and W. Thatcher, Coseismic slip resolution along a plate boundary megathrust: The Nankai Trough, Southwest Japan, *J. Geophys. Res., 104*, 1111-1129, 1999.

Satake, K., K. Shimazaki, K., Y. Tsuji and K. Ueda, Time and size of a giant earthquake in Cascadia inferred from Japanese tsunami records of January 1700, *Nature, 378*, 246-249, 1996.

Sato, T., and M. Matsu'ura, Cyclic crustal movement, steady uplift of marine terraces, and evolution of the island arc - trench system in Southwest Japan, *Geophys. J. Int., 111*, 617-629, 1992.

Savage, J. C., A dislocation model of strain accumulation and release at a subduction zone. *J. Geophys. Res., 88*, 4984-4996, 1983.

Savage, J. C., J. L. Svarc, W. H. Prescott, and M. H. Murray, Deformation across the forearc of the Cascadia subduction zone at Cape Blanco, Oregon, *J. Geophys. Res., 105*, 3095-3120, 2000.

Scholz, C. H., *The Mechanics of Earthquakes and Faulting*, 439 pp., Cambridge University Press, New York, 1990.

Shennan, I., A. J. Long, M. M. Rutherford, F. M. Green, J. B. Innes, J. M. Lloyd, Y. Zong, and K. J. Walker, Tidal marsh stratigraphy, sea-level change and large earthquakes; I, A 5000 year record in Washington, U.S.A., *Quat. Sci. Rev., 15*, 1023-1059, 1996.

Shennan, I., A. J. Long, M. M. Rutherford, J. B. Innes, F. M. Green, J, and K. J. Walker, Tidal marsh stratigraphy, sea-level change and large earthquakes; II, Submergence events during the last 3500 years at Netarts Bay, Oregon, USA, *Quat. Sci. Rev., 17*, 365-393, 1998.

Sugiyama, Y., Neotectonics of Southwest Japan due to the right-oblique subduction of the

Philippine Sea plate, *Geofis. Int., 33*, 53-76.

Tanioka, Y., and K. Satake, Coseismic slip distribution of the 1946 Nankai earthquake and aseismic slips caused by the earthquake, *Earth Planets Space, 53*, 235-241, 2001.

Thatcher, W., The earthquake deformation cycle at the Nankai Trough, Southwest Japan, *J. Geophys. Res., 89*, 3087-3101, 1984.

Trehu, A., T. M. Brocher, M. Fisher, K. Creager, L. Preston, G. Spence, and SHIPS98 Working Group, Geometry of the subducting Juan de Fuca Plate: New constraints from SHIPS98, in *Joint USGS/GSC Open File Report: The Cascadia Subduction Zone and Related Subduction Systems: Seismic Structure, Intraslab Earthquakes and Processes, and Earthquake Hazards*, Edited by S. Kirby, K. Wang, and S. Dunlop, in press, 2002.

Tsuji, Y., K. Ueda, and K. Satake, Japanese tsunami records from the January 1700 earthquake in the Cascadia subduction zone (in Japanese with English abstract), *Zisin (J. Seismol. Soc. Jap.), 51*, 1-17, 1998.

Tushingham, A. M., and W. R. Peltier, ICE-3G: A new global model of Pleistocene de-glaciation based upon geophysical predictions of post-glacial relative sealevel change, *J. Geophys. Res., 96*, 4497-4523, 1991.

Wang, K., Coupling of tectonic loading and earthquake fault slips at subduction zones, *Pure Appl. Geophys., 145*, 537-559, 1995.

Wang, K., Stress-strain "paradox", plate coupling, and forearc seismicity at the Cascadia and Nankai subduction zones, *Tectonophys., 319*, 321-338, 2000.

Wang, K., J. He, H. Dragert, and T. S. James, Three-dimensional viscoelastic interseismic deformation model for the Cascadia subduction zone, *Earth Planets Space, 53*, 295-306, 2001.

Wells, R. E., and R. W. Simpson, Northward migration of the Cascadia forearc in the northwestern U.S. and implications for subduction deformation, *Earth Planets Space, 53*, 275-283, 2001.

Wells, R. E., C. S. Weaver, and R. J. Blakely, Forearc migration in Cascadia and its neotectonic significance, *Geology, 26*, 759-762, 1998.

Wilson, D. S., Confidence intervals for motion and deformation of the Juan de Fuca plate, *J. Geophys. Res., 98*, 16,053-16,071, 1993.

Table 1. Terms used in this paper for fault behavior.

Expression	Explanation	Other often seen wording
locked	not slipping, regardless of fault property or stress	coupled; fully coupled; coupling ratio = 1
slip at plate convergence rate	self-explanatory; regardless of fault property or stress	decoupled; free slip; creep; coupling ratio = 0
slip more slowly than plate convergence	self-explanatory; regardless of fault property or stress	partially coupled; creep; coupling ratio between 0 and 1
slip faster than plate convergence	self-explanatory; regardless of fault property or stress	creep; coupling ratio > 1
coupled	shear stress $\neq$ 0, regardless of whether the fault is locked	
decoupled	shear stress = 0, regardless of whether the fault is slipping	
stable-sliding	a fault frictional property: resistive shear stress increases with slip rate; it in no way implies that sliding must be at the plate convergence rate	velocity-strengthening

Table 2. Euler poles involved in this paper's discussions.

Pole	Latitude (°N)	Longitude (°E)	Rotation Rate (°/Ma)	References
JDF-NA1	29.40	-111.70	-1.090	Riddihough [1984]
JDF-NA2	20.70	-112.20	-0.800	DeMets et al. [1990]
JDF-NA3	26.63	-110.45	-0.804	(from PA-NA and JDF-PA in this table)
PA-NA	51.50	-73.70	-0.765	DeMets and Dixon [1999]
JDF-PA	28.30	29.30	0.501[†]	DeMets et al. [1994]
forearc-NA	45.54	-119.60	1.316	Wells and Simpson [2001]
JDF-forearc	67.40	-147.94	0.627	(from JDF-NA and forearc-NA)

[†] The rate was mistyped as 0.520 in the original reference.

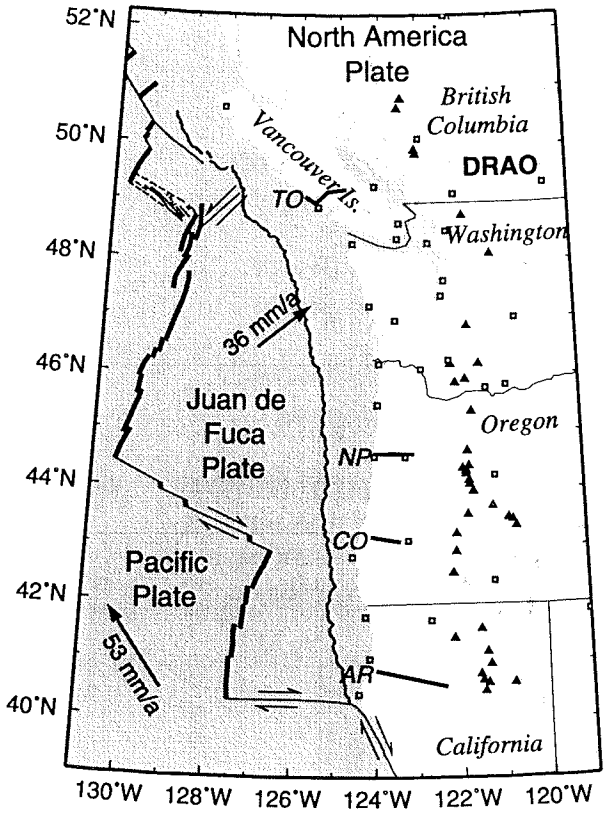

Figure 1. Regional tectonics of the Juan de Fuca ridge - Cascadia subduction zone system. Thick line segments - spreading ridge; thin linear segments: faults; thin curved line segments: Cascadia deformation front; solid triangles: active volcanoes; squares: continuous GPS sites, with DRAO being the reference site. Plate velocities (base on DeMets and Dixon [1999]) are relative to North America. Leveling lines: AR, Arcata-Redding line; CO, Coquille-Dillard line; NP, Newport-Albany line; TO, Tofino line.

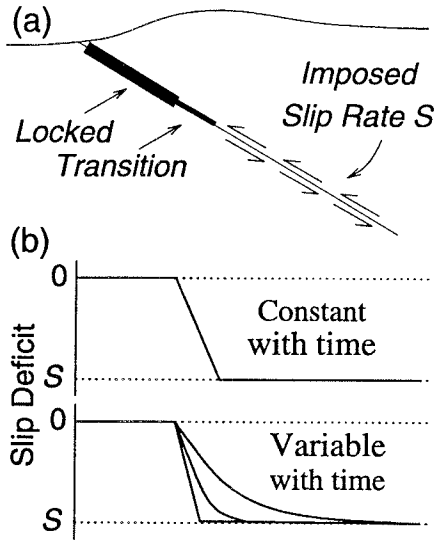

Figure 2. (a) The elastic dislocation model for subduction zone interseismic deformation. (b) A common assumption in the applications of this model is that a deeper portion of the fault slips at a constant rate, but in reality the slip distribution should vary with time.

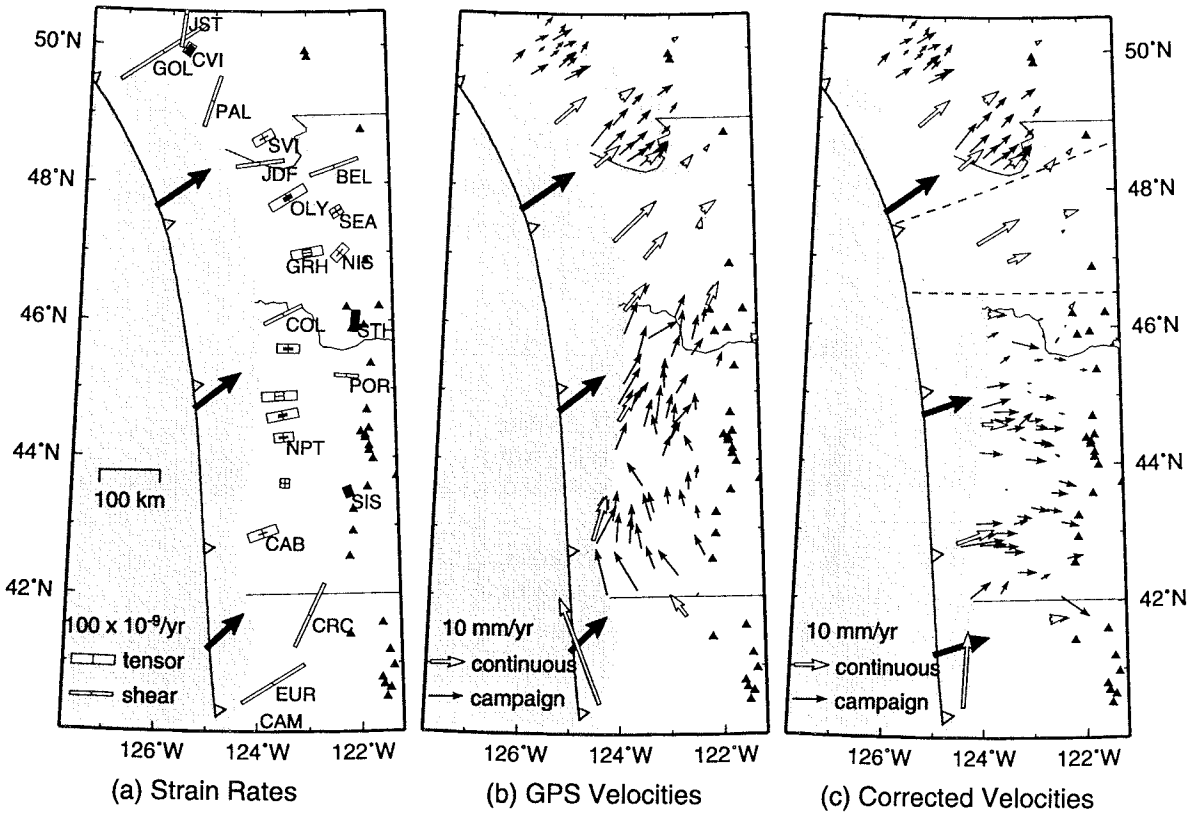

Figure 3. (a) A summary of geodetic strain rate measurements compiled from triangulation, laser ranging, and GPS observations. For strain rate tensor estimates, an open bar indicates contraction, and a solid bar indicates extension. Where only shear strain rates were determined, maximum contraction direction and rate are shown assuming uniaxial contraction. Each value represents an average over the area of the strain network used. (b) Summary of published GPS velocities in the Cascadia subduction zone. All velocities are relative to reference station DRAO in British Columbia (see Figure 1). (c) GPS velocities after a secular forearc motion is removed, as will be explained in Section 2.2. The remaining velocity field is considered to represent the elastic interseismic deformation. Vectors offshore show the direction of Juan de Fuca plate motion relative to North America in (a) and (b) but relative to Cascadia forearc in (c).

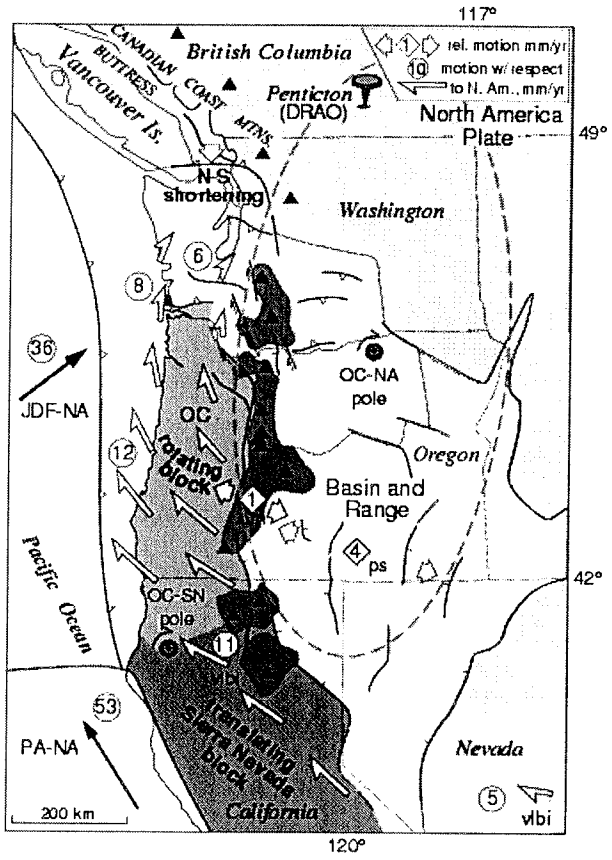

Figure 4. Forearc motion model of Wells et al. [1998]. Shown is an improved version by Wells and Simpson [2001] of the forearc motion rates (white arrows) relative to North America as defined by the OC-NA Euler pole. Oregon block (OC) rotating at Neogene paleomagnetic rate is linked by the OC-SN Euler pole to the Sierra Nevada block, itself rotating about a distant pole at a rate constrained by Very Long Baseline Interferometry (VLBI, Argus and Gordon, 1991) and GPS (Dixon et al, 2000).

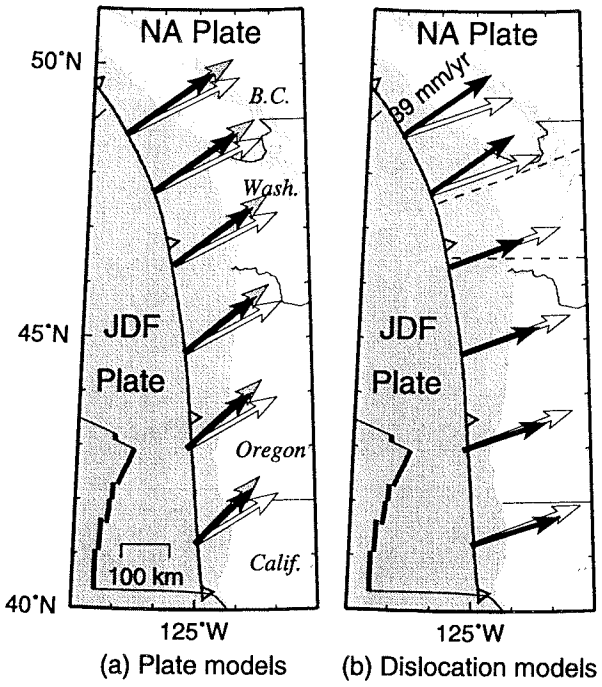

Figure 5. (a) Plate convergence vectors predicted by three Juan de Fuca - North America Euler poles (see Table 2 for pole positions and rotation rates). White arrows: NUVEL-1 model of DeMets et al. [1990]; grey arrows: Riddihough [1984]; black arrows: motion determined from the new Pacific - North America pole of DeMets and Dixon [1999] and the NUVEL-1A Juan de Fuca - Pacific pole [DeMets et al., 1994; Wilson, 1993]. (b) Plate convergence vectors assumed by CAS3D-1 (white arrows) and CAS3D-2 (black arrows). See Section 2.2 for explanation.

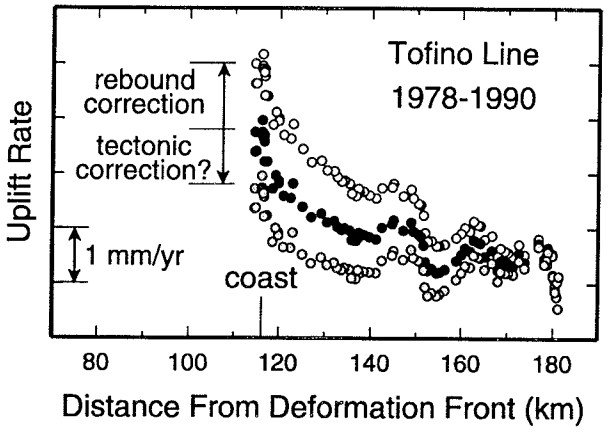

Figure 6. Uplift rates along the Tofino leveling line across Vancouver Island showing a land tilt (solid circles; data reported by Dragert et al. [1994]). The absolute level is arbitrary. The post-glacial rebound correction was made previously (open circles) but is no longer considered necessary. On the contrary, a correction for a long-term tectonic tilt may be necessary. Grey circles represent data corrected for a tilt rate of 1 mm/yr over the length of the profile. See Section 2.3 for details.

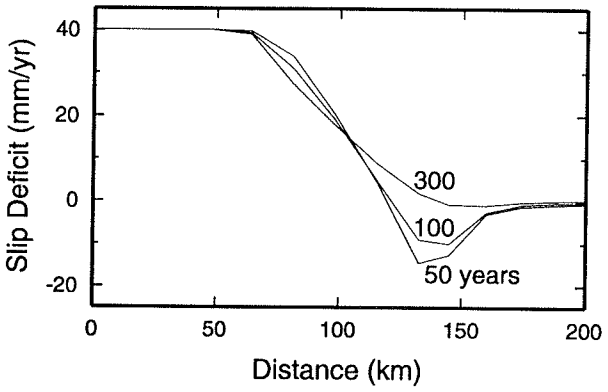

Figure 7. Slip deficit rates of the subduction fault along a profile across southern Vancouver Island at different times after a great earthquake from a 3-D viscoelastic model [Wang et al., 2001].

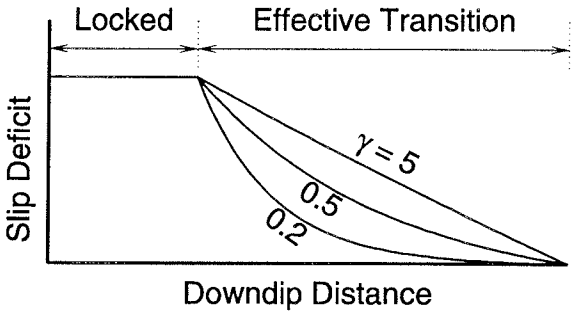

Figure 8. Slip deficit (backslip) distribution in the transition zone as defined by equation (1) for three different values of the shape factor γ.

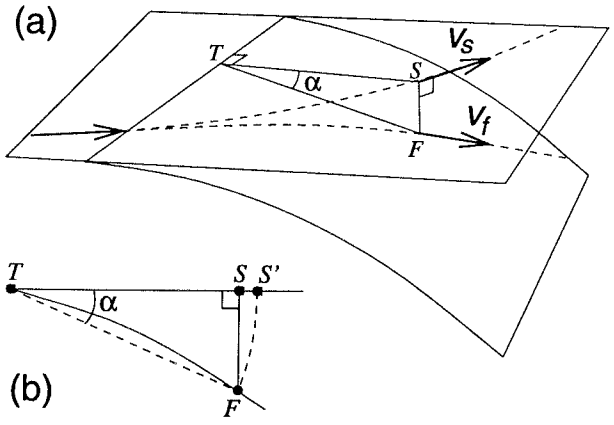

Figure 9. (a) Illustration of how the fault slip (or backslip) vector v_f is calculated from the surface convergence vector v_s using a small-dip approximation. (b) Illustration of how point S' is approximated using point S (see text for details).

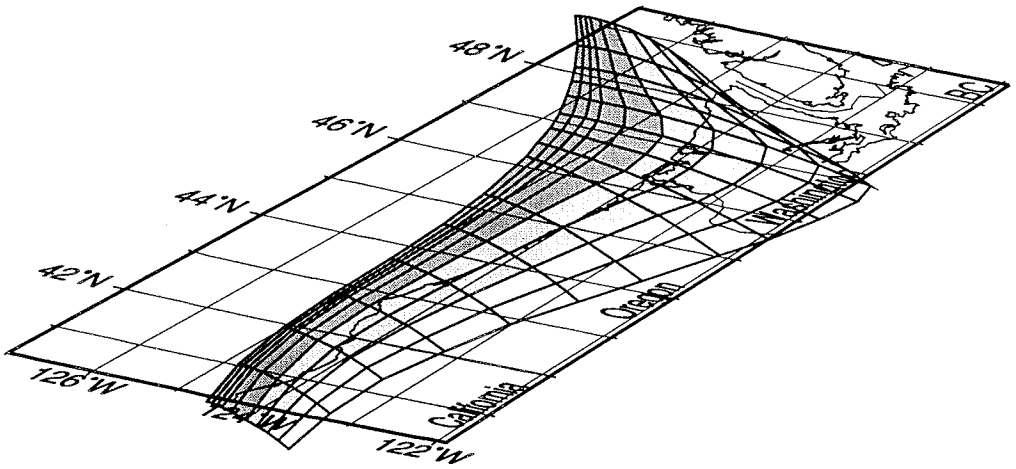

Figure 10. Perspective 3-D view of the locked zone and effective transition zone of the Cascadia subduction fault at present assumed by CAS3D-2. The transition zone is divided into two halves, and only the seaward half (intermediate shading) is involved in the calculation of potential coseismic deformation.

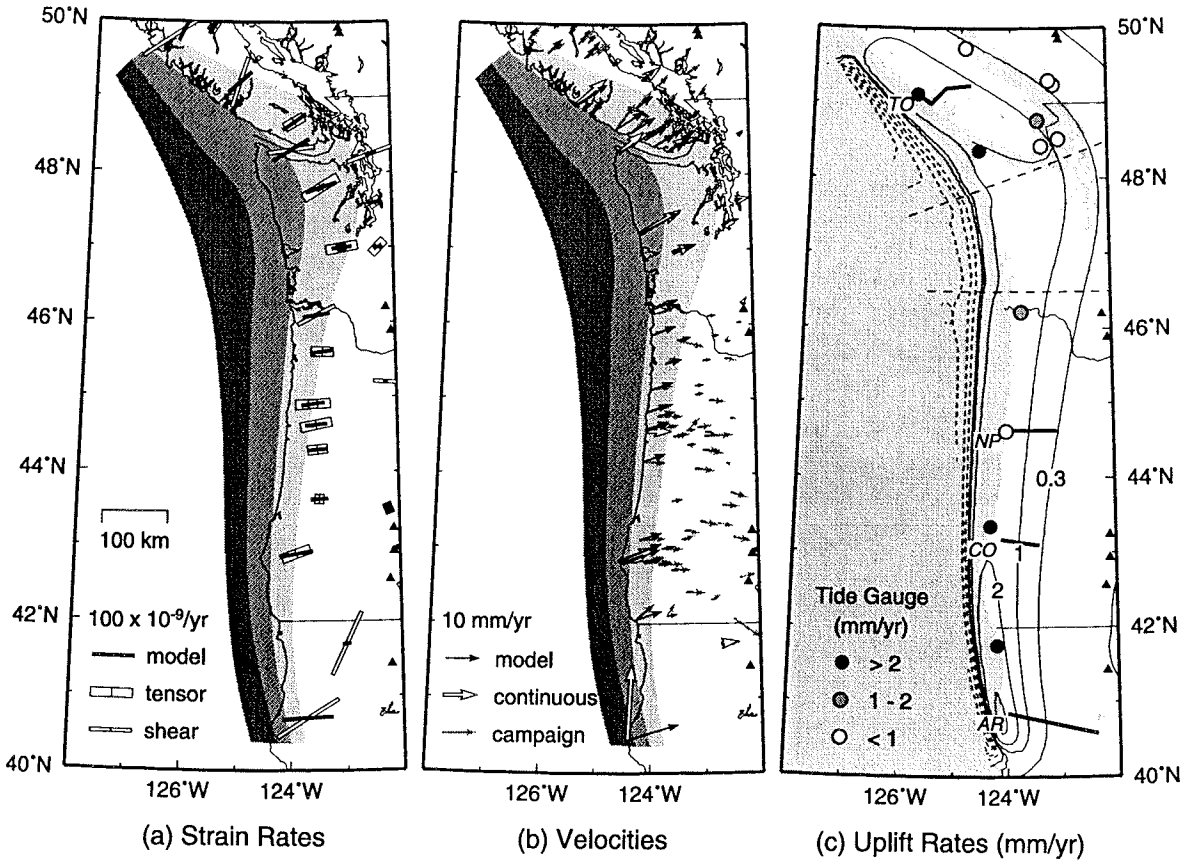

Figure 11. Model results of CAS3D-2 compared with geodetic observations. (a) Model and observed strain rates. The "tensor" strain rates are the best geodetic data constraints for an interseismic deformation model. (b) Model velocities and GPS velocities. GPS data for central and southern Cascadia have been corrected for secular forearc motion (Figure 3). (c) Model uplift rates (contour lines) and uplift rates derived from tide gauge records (see text for details).

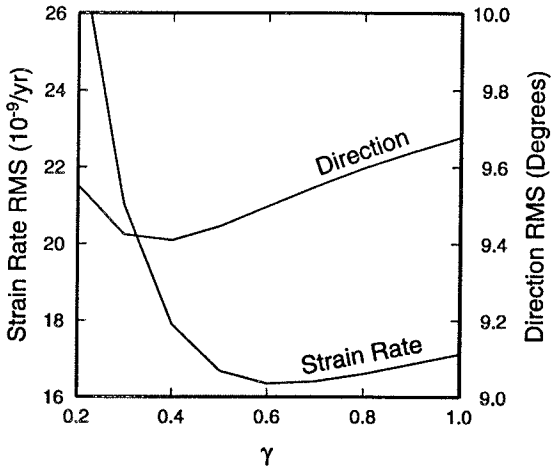

Figure 12. Root-mean-square (RMS) misfit of model predicted rates and directions of maximum contraction to strain rate tensor observations (excluding arc and backarc sites) as a function of shape factor γ (equation (1)) for the model geometry of Figure 10.

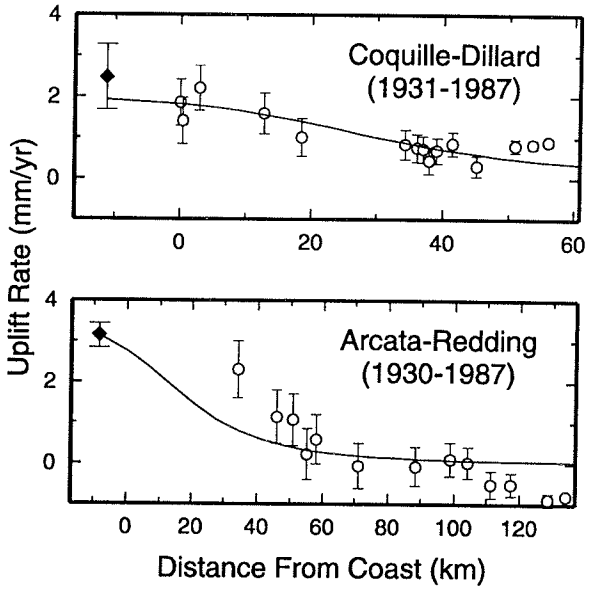

Figure 13. Model uplift rates (lines) compared with leveling data along two leveling lines (see Figure 3 for locations). Solid diamond represents uplift rate inferred from the tide gauge nearest to the leveling line.

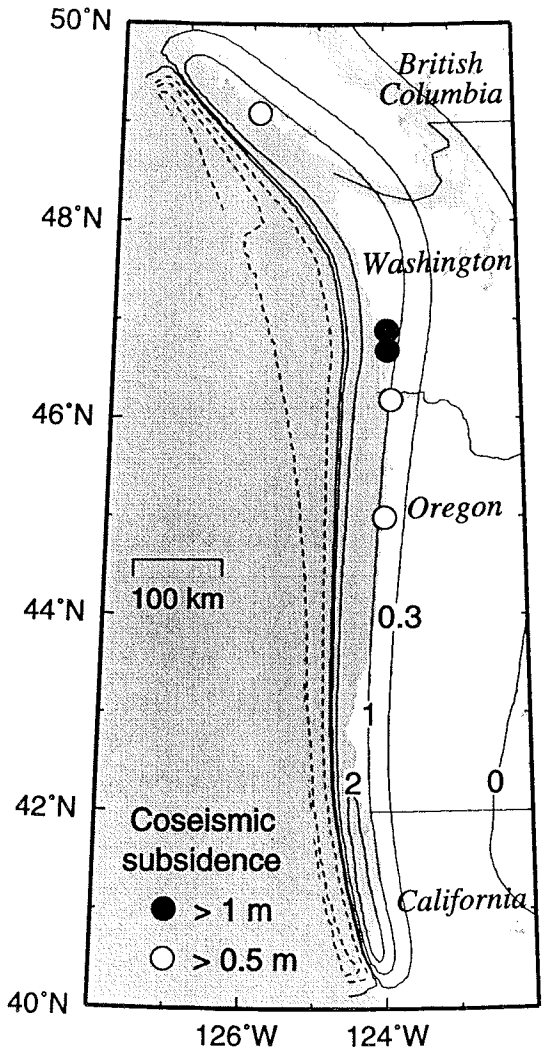

Figure 14. A coseismic deformation scenario assuming a full rupture of 18 m over the entire locked zone (dark shading in Figure 11a) with fault slip linearly decreasing to zero over the seaward half of the effective transition zone (intermediate shading in Figure 11a). See text for paleoseismic subsidence estimates.